analytical chemistry

pubs.acs.org/ac Article

Cell Phase Identification in a Three-Dimensional Engineered Tumor Model by Infrared Spectroscopic Imaging

Pei-Hsuan Hsieh, Yamuna Phal, Kannanganattu V. Prasanth, and Rohit Bhargava*

Cite This: https://doi.org/10.1021/acs.analchem.2c04554 Read Online

ACCESS | Metrics & More | Article Recommendations | Supporting Information

ABSTRACT: Cell cycle progression plays a vital role in regulating proliferation, metabolism, and apoptosis. Three-dimensional (3D) cell cultures have emerged as an important class of *in vitro* disease models, and incorporating the variation occurring from cell cycle progression in these systems is critical. Here, we report the use of Fourier transform infrared (FT-IR) spectroscopic imaging to identify subtle biochemical changes within cells, indicative of the G1/S and G2/M phases of the cell cycle. Following previous studies, we first synchronized samples from two-dimensional (2D) cell cultures, confirmed their states by flow cytometry and DNA quantification, and recorded spectra. We determined two critical wavenumbers (1059 and 1219 cm^{-1}) as spectral indicators of the cell cycle for a set of isogenic breast cancer cell lines (MCF10AT series). These two simple spectral markers were then applied to distinguish cell cycle stages in a 3D cell culture model using four cell lines that represent the main stages of cancer progression from normal cells to metastatic disease. Temporal dependence of spectral biomarkers during acini maturation validated the hypothesis that the cells are more proliferative in the early stages of acini development; later stages of the culture showed stability in the overall composition but unique spatial differences in cells in the two phases. Altogether, this study presents a computational and quantitative approach for cell phase analysis in tissue-like 3D structures without any biomarker staining and provides a means to characterize the impact of the cell cycle on 3D biological systems and disease diagnostic studies using IR imaging.

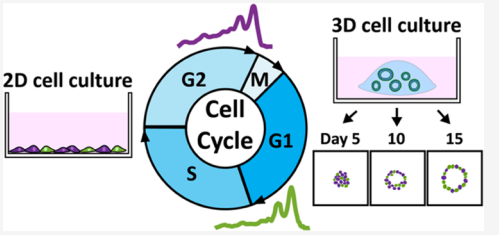

INTRODUCTION

Cell cycle progression can influence biochemical measurements from biological systems. Infrared (IR) spectroscopy and imaging[1,2] provide a label-free measurement of cellular biochemistry that dispenses with the need for dyes and stains to enable new insights,[3,4] help in diagnostic processes,[5] and evaluate the influence of the cellular microenvironment.[6] Spectral data can be routinely recorded at the single-cell level[7] in both culture and complex systems wherein heterogeneity is commonly considered to arise from distinctive biological signatures of cell type or diseased state.[8] Yet, a large spectral variance has also been reported between individual cells cultured under uniform conditions.[9−13] Since cellular proliferation is an active process, chemical components such as proteins and DNA evolve along with morphological changes throughout the cell cycle[14] and likely affect spectral data. Subtyping an ensemble of cells into relatively homogeneous subgroups based on the cell cycle (namely, G1, S, G2, and M phases) can help understand variance associated with cell cycle progression and facilitate analyses that consider it in studying cellular metabolism, biological response, and disease progression by IR spectroscopy.

Two-dimensional (2D) cell cultures are most commonly used for studies; however, 3D cultures have been shown to capture biological phenomena that better mimic *in vivo* behavior,[15,16] for example, as shown by organoid models.[17] Exposure to nutrients, mechanical and molecular impacts of cell−cell contacts, and the physiochemical microenvironment influence the cell cycle stage and differentiation. These features are distinctly different in 3D cultures and have shown to be more realistic and compelling models for studying cell development and cellular interaction with drugs. Several of these studies have used the MCF10A cell line, which is a nontumorigenic human breast epithelial cell line. The cell line also displays differences in morphological features between 2D and 3D cultures, forming a spherical and polarized arrangement in 3D that resembles human mammary ductal architectures while resulting in a planar cuboidal geometry in 2D culture.[18−20] To study cell cycle-associated heterogeneity in 3D cultures, organoids are typically required to be dissociated into homogenous cell suspensions and labeled with cell cycle-specific fluorescent probes.[21] For instance, fluorescence-activated cell sorting (FACS) can be used to capture temporal snapshots of cellular status, but spatial information is lost.[22,23] Tandem methods such as flow cytometry with fluorescence imaging[24,25] permit real-time

Received: October 15, 2022
Accepted: December 7, 2022

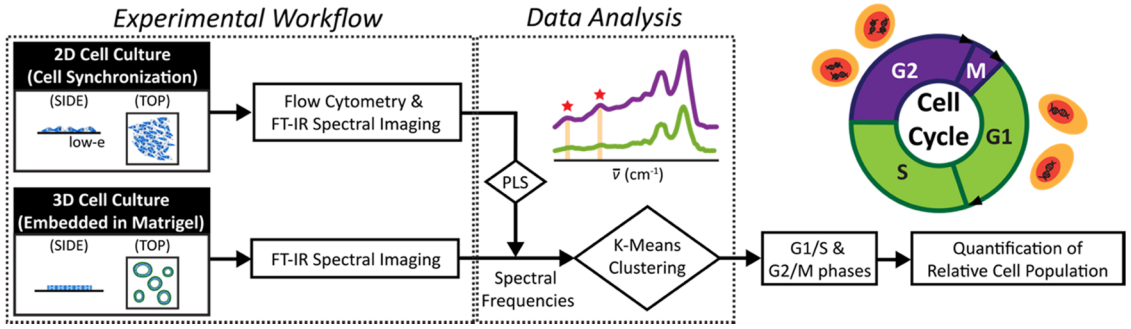

Figure 1. Experimental workflow, including synchronized 2D and 3D MCF10A cell cultures, sample preparation, and FT-IR spectral imaging. The subsequent data analyses are also shown in the flow chart.

observation of cell phases with the use of machine learning-based classification.[26] While these approaches have enabled new platforms for accurate label-free cell phase identification, examining both cell status and biochemical content from a spectroscopic perspective combined with multivariate analysis has also been an extensive topic.[9,10,27−32]

IR spectroscopy detects characteristic vibrational modes of indigenous molecules and provides a ready means to monitor cell physiology without the need for stains or dyes. Prior works have recorded high-quality spectroscopic data,[33−35] high-resolution profiling,[36,37] and subcellular measurements of single cells to quantify composition in the major classes of biological molecules,[38] even in live cells.[39] However, applications specific to cell cycle analysis have received less attention, and a vast majority of studies reported thus far have focused on 2D cultures. Only a few studies have investigated 3D cultures.[40−43] We sought to investigate IR spectra from 3D culture models to understand their compositions in terms of the cell cycle and estimate the impact of the cell cycle on heterogeneity. Our approach is to use 2D synchronized cultures, confirmed by cell sorting techniques, to record characteristic spectra during the cell cycle using Fourier transform infrared (FT-IR) spectroscopic imaging. Using these data, we then apply FT-IR imaging to understand heterogeneity in acini of MCF10AT series in 3D cell cultures. While IR spectroscopy has been used to study 2D cell cultures, the methods to be developed for observations within the innate microenvironment can be valuable as 3D cultures are rapidly gaining popularity for biomedical analyses. The cell cycle is an important parameter in the response of these cultures to drugs, for example; hence, quantitatively understanding the effects of cell proliferation and division via IR spectra in MCF10A acini can be fruitful.

MATERIALS AND METHODS

Cell Culture. The MCF10AT system, which is composed of four isogenic cell lines, was selected to represent the evolution of progressive breast cancer.[44] MCF10A and MCF10AT1k.cl2 (M2) cells were maintained in 75 cm^2 flasks in DMEM/F12 medium (Gibco #11320033) supplemented with 5% horse serum (Gibco #16050114), 20 ng/mL epidermal growth factor (Sigma 5036), 0.5 mg/mL hydrocortisone (Sigma H0888), 100 ng/mL cholera toxin (Sigma C8052), 10 μg/mL insulin (Sigma I1882), and 1% penicillin−streptomycin (Fisher I7602E). MCF10CA1h (M3) and MCF10CA1a.cl1 (M4) cells were maintained in DMEM/F12 medium supplemented with 5% horse serum and 1% penicillin−streptomycin. The cells were cultured in a 5% CO_2 incubator at 37 °C and passaged at 70% confluency. The passage number was subjected to less than eight in the experiments to avoid any genetic drift.

Sample Preparation. The pipeline for experiments and spectral analyses reported here is illustrated in Figure 1. A 2D cell culture of the MCF10AT cell series was directly seeded on UV-sterilized MirrIR low-e reflective microscope slides (Kevley Technologies) at a density of 5 × 10^5 cells/mL. The cell seeding density was carefully controlled such that the cells were deposited as a monolayer to prevent cell aggregates. Cell aggregates are not desirable since they result in the distortion of IR microscopy spectra due to multiple scattering and other effects.[11,45] Cells were cultured for 24 h until they attached onto the substrate. Finally, these asynchronous cells were either fixed as a control group or further synchronized to G1/S or G2/M phases. The details of cell cycle synchronization are described in the Supporting Information.

All four cell lines were cultured using a 3D protocol.[46] Cells were suspended evenly in growth factor-reduced Matrigel (Corning #356231) at a density of 2.5 × 10^4 cells/mL. Cell-embedded Matrigel was deposited onto a 12-well cell culture plate, and it underwent gelation under 37 °C. Each pellet was then detached from the bottom to prevent any external mechanical stiffness from the well. The culture duration was 15 days, and the medium was replaced every 2−3 days. The diameter of the acini was measured by Fiji[47] from the images taken across different wells. Cell-embedded Matrigel pellets were washed with phosphate-buffered saline (PBS) and flash-frozen in optimal cutting temperature (OCT) compound at days 5, 10, and 15. The frozen blocks were cryosectioned (Leica CM3050S) at 5 μm thickness and collected on either low-e slides for FT-IR imaging or glass slides for hematoxylin and eosin (H&E) and immunofluorescence staining. All the samples were fixed with 4% paraformaldehyde (PFA) overnight at 4 °C and quenched with 0.15 M cold glycine solution for 1 h. Each step was followed by three PBS washes to remove the residual OCT and Matrigel, which turned into liquid state at 4 °C. Therefore, the potential interfering effect of OCT and Matrigel during the IR measurement is not considered in the study. Samples on low-e slides were additionally rinsed by diH_2O to remove residual PBS from their surface and dried by nitrogen purging overnight prior to FT-IR imaging.

FT-IR Spectroscopic Imaging. Samples on low-e slides, which are stored in a nitrogen-purged environment, were imaged using a 680 FT-IR spectrometer coupled to a 620-IR imaging microscope (Agilent Technologies). The system is equipped with a high-throughput 15× Vis/IR objective and a liquid nitrogen-cooled 128 × 128-pixel focal plane array (FPA)

https://doi.org/10.1021/acs.analchem.2c04554
Anal. Chem. XXXX, XXX, XXX−XXX

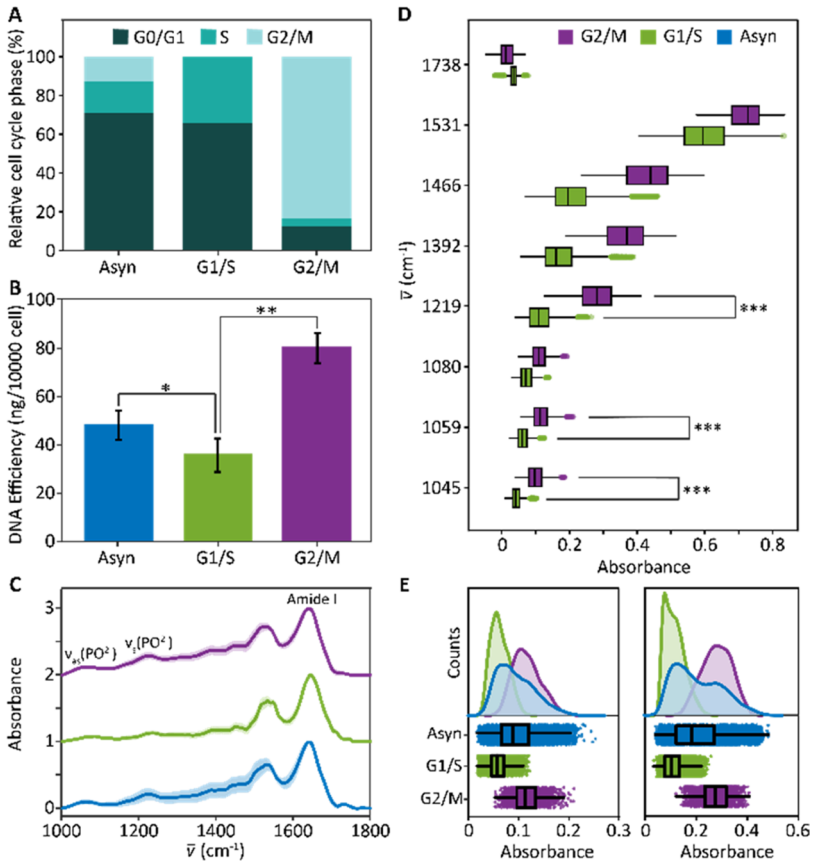

Figure 2. Validation of cell synchronization and IR spectral signatures associated with intracellular DNA levels. (A) Flow cytometry assessment of intracellular DNA content of cell samples. (B) Quantification of extracted DNA from different cell phases. (C) Average IR spectra of cells recorded from asynchronous (blue), G1/S arrested (green), and G2/M arrested (purple) phases. Standard deviation is marked as the shaded area. (D) Absorbance visualization with wavenumber as categorical labels to identify the most significant spectral bands that distinguish between cell phases, with absorbance at (E) 1059 cm^{-1} (left) and 1219 cm^{-1} (right) showing significant differences but considerable overlap as well. For the Box–Whisker plots in panels (D) and (E), the top and bottom edges correspond to the first and third quartiles and the midline represents the sample median. The upper and lower whiskers extend from the hinge up to 1.5× IQR. Outlier values are indicated if they extend beyond this range.

mercury–cadmium–telluride (MCT) detector with a 5.5 × 5.5 μm^2 pixel size. The measurement was acquired in "high magnification," which increased the effective pixel size to 1.1 × 1.1 μm^2.[48,49] For each mosaic image, 6 × 6 tiles were captured in an epi-illumination configuration with 256 coadditions at an undersampling ratio of 4 and truncated to 800–3900 cm^{-1} at 4 cm^{-1} spectral resolution. The data were corrected against the background, an empty area on the same slide whose single beam data were acquired using 512 coadditions.

IR Data Analysis. Datasets spanning the fingerprint region, 1000–1800 cm^{-1}, were processed using minimum noise fraction (MNF) built-in Environment for Visualizing Images Interactive Data Language (ENVI-IDL). Next, Otsu thresholding segmentation was applied to the absorbance images at Amide I (1650 cm^{-1}) to define the region of interest (ROI). Pixel-wise spectra were extracted from the corresponding pixels in the foreground expression[50] and were refined by means of baseline correction, followed by Savitzky–Golay smoothing, density-based clustering (dbscan), and normalization to the maximum value at the Amide I peak in MATLAB R2020a.

The relation between the spectral absorbance and the cell phase is complex. Partial least-squares (PLS) regression, a multivariate data analysis method, was utilized to identify bands that show the most significant contrast in distinguishing between G1/S and G2/M phases. Specifically, PLS overcomes the collinearity problem of ordinary least-squares regression by analyzing and extracting principal components and quantifying the relation using regression scores. Hence, the PLS method is ideal for our problem of modeling the cell phases with multiple dependent variables (wavenumber).[51]

Next, ANOVA was performed on the selected bands, and the statistical significance between various groups was evaluated. Two wavenumbers that showed the lowest p-value were identified as representatives to quantitatively map the relative amount of DNA change between the cell phases. Based on the identified wavenumbers, K-means clustering, an unsupervised pixel-wise classification method, was used to minimize the within-cluster variances. The data points from the sectioned 3D samples were partitioned into two clusters, representing the G1/S and G2/M phases.

RESULTS AND DISCUSSION

Analysis of Cell Cycle Phases. Figure 1 shows the overall design and workflow which was implemented in this study. Both 2D and 3D cell cultures were prepared and data was recorded, as described in the Materials and Methods section. We first consider experiments in the context of the cell cycle. During the G1 phase, the cell prepares for DNA replication and moves on to the S phase (2–4 N), where DNA is duplicated. In the subsequent G2 phase (4 N), the microtubule

https://doi.org/10.1021/acs.analchem.2c04554
Anal. Chem. XXXX, XXX, XXX–XXX

structure is rearranged and the cell proceeds to cell division. Finally, the cell undergoes mitosis (M phase) and either shifts to a quiescent state (G0) or re-enters the G1 phase. To reduce spectral variations in asynchronized conditions, 2D cultured cells were first arrested at two predetermined cell phases, G1/S and G2/M. Since different cell types are regulated by their distinctive mechanisms, protocols for cell synchronization need to be specifically optimized. Thymidine, a DNA synthesis inhibitor, and nocodazole, a microtubule inhibitor, were chosen to arrest the cells prior to the G1/S and G2/M phase boundaries, respectively. Asynchronized cells without any chemical treatments served as the control. To validate that the cells were effectively arrested, flow cytometry was used to quantify the cell distribution in each phase. As shown in Figure 2A, in the control group, the cell population distribution across G1, S, and G2/M phases was 71.3, 16, and 12.7%, respectively. In the group treated with double-thymidine block, nearly 100% of the cells were arrested in the G1/S phase prior to DNA duplication. On the other hand, the group treated with nocodazole had 83.6% of the cell population arrested in the G2/M phase. Cross-validation was provided by quantifying isolated DNA from the corresponding groups (Figure 2B), showing a distinct quantitative difference between the G1/S and G2/M phases. For the control group, the mean DNA efficiency was 48.69 ng per 10 000 cells, whereas for G1/S and G2/M phases, the values were 36.43 and 80.78 ng per 10 000 cells, respectively. This trend is consistent with that of flow cytometry results, and the synchronization protocol for controlling the cell cycle was verified.[52]

A significant absorbance variation within single batches of a monolayer cell culture[53] was observed and has previously been reported.[12] One reason is the scattering from morphological structures that are at the same length scales at the wavelength of light.[11,13,54,55] This typically manifests in spectra as small shifts in peaks and a dominant, wavelength-dependent baseline offset,[56] which continues to remain a topic of interest in modeling and understanding IR data recorded from a microscope. Another source of spectral heterogeneity in homogeneous monolayer cell cultures can be attributed to cells equilibrating to cell cycle phases during development or disease progression. Thus, it results in a varied composition within an ensemble of cells.[57] Our results show that this equilibrium can be a source of variation and will be useful to examine whether the same equilibrium is attained in 3D cultures. Before we examine 3D cultures, we fully characterize the spectral properties of 2D cultures.

Spectral Characteristics of Cell Cycle Phases. Since the amount of nucleic acid and other constituents vary during the cell cycle, we examined whether cells arrested in G1/S and G2/M phases also show differences in IR absorption spectra. FT-IR spectroscopic imaging data were obtained (Figures S1 and S2) for each condition, and spectra were normalized to Amide I vibrational mode (Figure 2C). For an initial assessment, we used partial least-squares (PLS) analysis to determine spectral features that allow segmentation of the data by cell phase. Interestingly, the spectral frequencies with relatively higher PLS weights lay in the 1020−1080 and 1150−1270 cm^{-1} ranges. These are typically attributed to the symmetric and asymmetric stretching of the phosphate groups (PO_2^-), respectively, which are found on the backbone of nucleic acid (DNA and RNA), phospholipids, and phosphorylated proteins (Figure 2D).[58−61] The symmetric stretching band of phosphates ∼1083 cm^{-1} was found in both asynchronized and synchronized groups. This peak is associated with all forms of nucleic acids, including RNA, ss-cDNA, and ds-DNA.[27] In contrast, within the spectral range 1150−1270 cm^{-1}, the center of the peak attributed to the asymmetric phosphate stretching mode shifts from 1232 to 1224 cm^{-1} while proceeding from G1/S to G2/M phases.[27] A possible cause of this shift can be the DNA conformation transition between A (1240 cm^{-1}) and B forms (1225 cm^{-1}).[60] Moreover, it is reported that RNA contributes nearly half of the nucleic acid content during the active cell cycle,[62] which may also influence the shift of the peak location. To further confirm the assignment of these peaks, IR spectra on extracted DNA from the corresponding cells were acquired by an ATR accessory equipped FT-IR spectrometer (Figure S3). The spectra displayed several major peaks at 965 (ν(C−C)), 1049 (ν(C−O)), 1082 ($\nu_{sym}(PO_2^-)$), and 1216 cm^{-1} ($\nu_{asym}(PO_2^-)$) (all ±2 cm^{-1}), which are generally regarded as peaks associated all of the nucleic acid forms.[27,63] Also, these peaks match the peak assignments of an isolated double-stranded DNA sample in the previous study.[27] An additional peak is identified as a shoulder at ∼936 cm^{-1}, which is attributed to the AT base pairs vibration of B-DNA helices.[64] As previously mentioned, there is a possibility that RNA remains in the cells and contributes to the IR signal. However, in our result, the particular peaks referred to ribose rings of RNA are not observed in the isolated DNA spectra, which are at the hydroxyl group at C2′ at 1125 and 993 cm^{-1} and C−C ring vibration at 914 cm^{-1}.[64,65] As our sample preparation protocols did not include RNAse-free conditions, the contribution of RNA in the spectra is not discussed in this study. In principle, the spectral differences between the phases should correspond to a 2-fold higher DNA absorbance in the G2/M phase data compared to that from the G1/S phases. In Figure 2E, the absorbance at 1059 and 1219 cm^{-1} shows a cell stage-dependent difference, whereas the asynchronized group lies in the middle with a wide range across the absorbance from both the synchronized groups. Chemical images plotting the absorbance at 1219 cm^{-1} (Figure S1) show lower relative absorbance at G1/S compared to the G2/M phase. The acquired absorbance measurements at 1219 and 1059 cm^{-1} served as input parameters in the ANOVA analysis. The p-values are very close to 0, which indicates that the absorbance difference between G1/S and G2/M phases is statistically significant. Furthermore, we estimate the mean absorbance at 1219 and 1059 cm^{-1} for each group of cell phases, along with the standard errors in the estimate. The 95% confidence interval lies within an absorbance of 10^{-3}, which is within the noise limits of the current state-of-the-art measurements. Based on these results, it appears that the absorbance at 1219 and 1059 cm^{-1} can be used as an effective indicator[66] to distinguish between G1/S and G2/M phases in further experiments.

Transitioning from 2D to 3D Cell Cultures. 3D cultures have been relatively less studied by IR imaging[42,43,67−71] due to the additional challenges in the 3D cell culture system, including culture reproducibility, challenging sample post-processing, and lack of protocols for interpretation. Communication between cells in a 3D ensemble and their micro-environment plays a pivotal role in regulating cell organization and function, and MCF10A, in particular, has been studied extensively using different culture methods.[46] Here, we adopted a "cell-embedded" method instead of an "on-top" one[46] since we sought to maximize the possibility of obtaining cells in each physical section afterward (Figure 3A). Initially,

https://doi.org/10.1021/acs.analchem.2c04554
Anal. Chem. XXXX, XXX, XXX−XXX

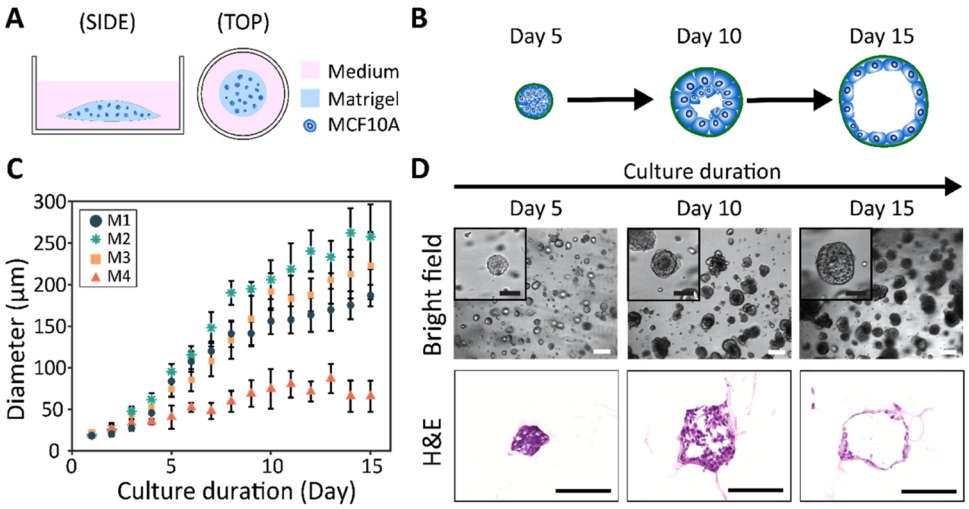

Figure 3. (A) Experimental setup for the MCF10A 3D culture. (B) Systematic figure of MCF10A acini formation under 3D cell-embedded conditions. (C) Size variation of M1 to M4 acini throughout 15 days of culture. (D) (Top row) Bright-field image of MCF10A acini formation at days 5, 10, and 15 of culture. Scale bar (white): 200 μm; inset diagrams show zoomed-in images of the acinus. Scale bar (black): 100 μm. (Bottom row) H&E-stained images of cryosectioned acini fixed at days 5, 10, and 15 of culture. Dark purple and pink stains indicate the nucleus and cytoplasm, respectively. Scale bar: 200 μm.

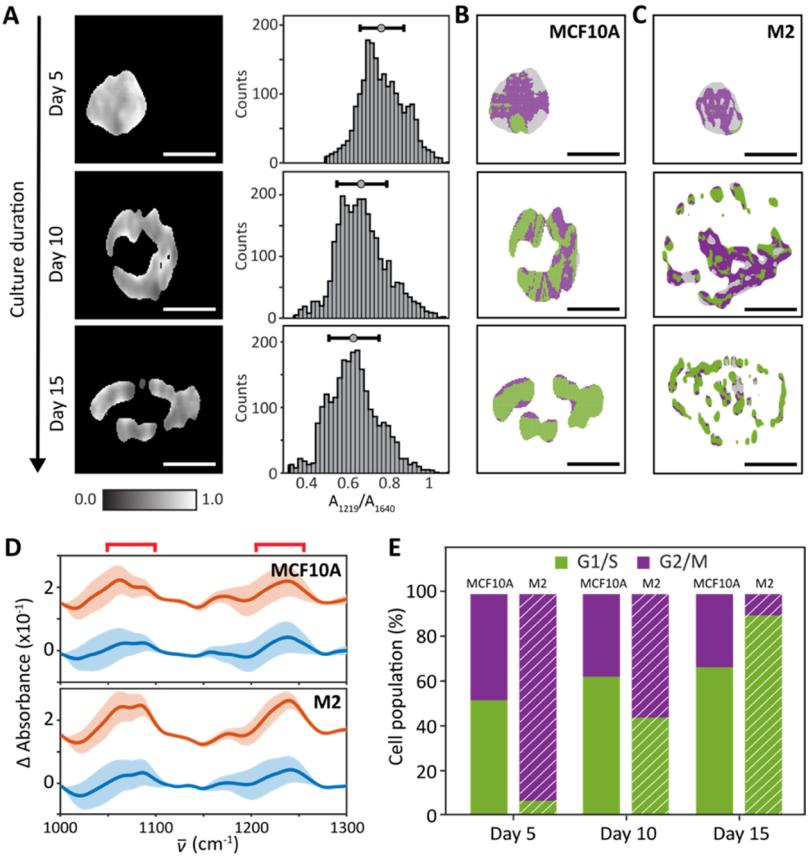

Figure 4. Label-free identification of cell phases in a single acinus. (A) Chemical images of cryosectioned acini shown for the ratio of absorbance at 1219−1640 cm^{-1} and acquired at days 5, 10, and 15 during the 3D cell culture duration. Scale bar: 50 μm. Corresponding intensity histograms are shown with the median and interquartile range above. The medians are 0.7559, 0.6794, and 0.6416, respectively, on days 5, 10, and 15. (B, C) Virtual staining of MCF10A and M2 acinus based on K-means clustering. Green, purple, and gray colors refer to G1/S, G2/M, and outliers, respectively. Scale bar: 100 μm. (D) Difference in absorbance spectra for days 5 and 10 and days 5 and 15. The blue line shows the difference between days 5 and 10, while the orange line shows the difference between days 5 and 15. The shaded areas present the standard deviation. (E) Analysis of the cell population in G1/S and G2/M phases for single acini at days 5, 10, and 15 for MCF10A cells (solid color) and M2 cells (solid color with white stripes). For MCF10A, the fraction of the cells in the G1/S phase changed from 51.9 to 66.73% during 15 days of culture. On the other hand, for M2 cells, the fraction of the cells in the G1/S phase has a more drastic shift from 6.34 to 90.24%.

https://doi.org/10.1021/acs.analchem.2c04554
Anal. Chem. XXXX, XXX, XXX−XXX

MCF10A cells were evenly distributed in Matrigel, which is mainly composed of laminin and collagen type IV. Single cells locally proliferated into an individual cell aggregation and eventually formed into acini with a hollow lumen structure, which mimics the breast epithelium seen in humans (Figure 3B). To observe the maturation of acini, the system was cultured for 15 days and cryosectioned. The size of the MCF10A acini increased and reached a plateau of around 190 μm in diameter on day 13 (Figure 3C). As expected, the cells in the core region underwent apoptosis, while the peripheral cells developed apicobasal polarity by self-arranging into hollow structures. Since M2 and M3 cell lines were transformed from the MCF10A cell line into higher proliferative and tumorigenic phenotypes, their acini showed a more rapid growth rate. On the other hand, as the M4 cell line is representative of the metastatic stage, it has limited capability to form acini (Figure S4). Bright-field and H&E-stained images reveal the structural organization of acini throughout their development (Figures 3D and S5).

We sought to study the temporal progression of the cell subpopulations in distinguished cell stages in a 3D MCF10A acini model. 3D cell cultures were conducted in triplicate to assess reproducibility, and FTIR imaging data were acquired for samples from days 5, 10, and 15 of the culture to capture the acinar differentiation process. Chemical images, represented by a ratio of the absorbance at 1219 cm^{-1} to that at 1640 cm^{-1}, can also be used to extract corresponding histograms, as shown in Figure 4A,B. The median values for the ratio are 0.7559, 0.6794, and 0.6416, respectively, on days 5, 10, and 15.

Next, we used Kolmogorov−Smirnov test statistics to evaluate the difference between these derived histograms. At the 1% significance level, the null hypothesis that the derived ratio distributions are from the same set of measurements is rejected with a p-value of about $\sim 10^{-24}$. The test statistic for days 5 and 10 and days 5 and 15 is 0.3769 and 0.4912, respectively, which is indicative of a higher deviation of the cumulative distribution function (in this case, day 5). It is notable that these spectra have lower variability compared to the 2D cell culture, which was surprising. We hypothesize that this might be due to sample surface variation of the 2D culture as well as biochemical variability from adhesion, varying neighbors, or surface differences in the underlying substrates. Many of these factors are absent in the sectioned (more uniform) samples from 3D culture. Before examining the spectral data, we note that the relative positions of cells are maintained here in images, whereas the traditional methods for cell cycle analysis, such as cell sorting and immunoblotting, result in a loss of information regarding the relative spatial arrangement. Chemical analyses by staining with fluorescent probes and antibody conjugation can also provide such information but could be challenging for the small volume of embedded cells and require a priori knowledge of the changes, though such analyses could be conducted on intact models using optical sectioning.

Since the major biological alterations take place in nuclei during the cell cycle, we focused specifically on characterizing DNA quantity. Based on the PLS results (Figure 2D), we used the absorbance at 1058 and 1219 cm^{-1} to help identify the abundance of G1/S or G2/M phases. We first projected this ratio back onto the images (Figure 4B) and saw a trend. The baseline corrected absorbance at 1058 cm^{-1} reduced from day 5 to day 10 by 21.38% and then to day 15 by 32.8%. Similarly, the absorbance at 1219 cm^{-1} reduced by 17.16% from day 5 to day 10 and then from day 10 to day 15 by another 32.54%, which is indicative of the cell phase shift from G2/M to G1/S phase (Figure S6B,C). Spectral differences between the culture durations can also be observed. There are two obvious peaks around 1040−1100 and 1200−1270 cm^{-1}, which are typically considered to arise from DNA. A similar trend of spectral features was also discovered in the data points from the M2 cell line, which is H-Ras mutated from the MCF10A cell line. A decrease in the absorbance at 1058 and 1219 cm^{-1} was seen while with a more prominent absorbance change comparing different stages of acini maturation. (Figures 4D and S7B,C). This reflects a more proliferative behavior, which matches the higher growth rate shown in Figure 4C. Next, K-means clustering was performed to partition the absorbance at 1058 and 1219 cm^{-1} into two groups, G1/S and G2/M phases (Figures S6D and S7D). Here, we consider the G1/S phase as a dormant state and G2/M as a progressing state. Interestingly, the fraction of cells in the G2/M phase was highest at day 5, which indicates a predominance of proliferative cells during the early development of acini. This fraction at day 15 for MCF10A is marginally lower than that found in the asynchronous 2D cell culture. Moreover, we hypothesize that the availability of nutrients confers this distribution of proliferative cells in acini. These data pixels were then projected back on the image to show the relative distributions of cells. In Figure 4C, by plotting the virtual staining based on the K-means clustering, those points categorized as the G2/M phase were most likely to present at the peripheral regions at the late stage of acini maturation, which can be explained by the direct contact with the matrix and higher exposure to nutrients.[20] The histogram plot of the K-means clustering result is presented in Figure 4E. With the increase of the culture period, the data points categorized into the G1/S phase increased, which indicates the stability of the acini maturation.

Biological Correlates and Variation with Tumor Progression Models. To further validate our results, a protein biomarker, Ki-67, for assessing proliferative cells was used. Our spectral analysis correlates with Ki-67 expression. This expression elevates when the cells arrive at the boundary of the G2 and M phases[72] and is known to decrease with the development of acini.[73] Ki-67 was markedly visible at the early stages of the cell culture, while after 3 weeks of culturing, the biomarker was barely detected. A possible explanation for this behavior of the cells being less proliferative is associated with the external mechanical constraints and specific oncogene expressions.[74] Typically, acini structure formation mirrors normal human breast glands.[75] When the cell and matrix anchoring is disrupted as a key step in cancer progression, a further molecular change may be noticed. To assess this characteristic, similar analyses were also performed on M3 cell lines as a model for *in situ* ductal carcinoma. In M3 acini, we did not observe a clear pattern to cell subpopulations, and composition in acini fluctuates without a clear growth pattern (Figures S8 and S9). This likely reflects a mix of populations between more M2-like states, intermediate progression states, and invasive and migratory states of the M4 subtype. The M4 cell line does not form into acini, representing the lack of coordination between cells and loss of adhesive behavior, and cannot be easily characterized in the same terms as the other three cell lines. It is possible that cells lie in the quiescent/senescence state as discussed in a previous study;[28] however,

https://doi.org/10.1021/acs.analchem.2c04554
Anal. Chem. XXXX, XXX, XXX−XXX

here, they were grouped into the G1/S phase based on the synchronization protocol for 2D cell cultures.

DNA Quantification Using IR Spectroscopy as a Biomarker. The recording of nucleic acid spectral features from cells has been a debated topic and also relates to the ability to detect subtle DNA changes during cell cycle progression. A "black string/dot" hypothesis has been proposed regarding the chromatin folding architecture within the nucleus that results in a lower value than the expected absorbance.[5,30,76] Our results are in agreement with more recent studies, which posit that nucleic acid, DNA specifically here, can be treated as a qualitative and semiquantitative biomarker on a single-cell basis to distinguish the cell stage.[28,29] To discover the correlation of DNA abundance with respect to DNA duplication and split, flow cytometry is commonly used as a complementary method to support findings from IR measurements.[28,29,40] The absorbance of the phosphodiester peak was found to positively correlate with cell cycle progression from G1 to G2/M phases either in hydrated living or dehydrated fixed cells.[28,29,77] For better reliability of spectral interpretation of DNA conformation, detailed investigations on various factors, including nucleotide composition, hydration, salt concentration, and counter ion, toward DNA conformation have been undertaken.[58,59] These results indicate that with carefully designed experiments and sample preparation protocols, IR spectroscopy has the capability to monitor subtle DNA changes with respect to the cell cycle. To link *in vitro* studies with physiological conditions, combining customized platforms with IR microscopes could provide more perspectives, even at the single-cell level.[40,78] Overall, the extensive understanding of the phosphodiester peak (PO_4^{2-}) position and intensity could serve as a promising tool in 3D cultures to provide further information about the dynamics of the nucleus and protein architecture while enabling important relations with clinical studies.

CONCLUSIONS

We report the use of FT-IR imaging as a nondestructive and label-free tool to investigate the relative DNA quantity differences throughout the cell cycle progression for 3D cell cultures using isogenic cell lines as models of cancer progression. Observations show that cell populations can be segmented into G1/S and G2/M phases, which represent a low and high degree of proliferative level for cell conditions, respectively. Extending the spectral signatures obtained from the analyses of 2D monolayer cell cultures to 3D cultures, IR spectral data could recognize the relative populations and changes with progression models cell cycle compositions in breast cancer organoids. We anticipate that the analysis could be used as a starting point to understand the role of the cell cycle in both model systems and tissues. Further development of this concept could pave the way to investigate highly complex systems with multiple compartments, including different cell types and microenvironments for fundamental studies such as drug-cell interactions and for digital histopathology.

ASSOCIATED CONTENT

Supporting Information

The Supporting Information is available free of charge at https://pubs.acs.org/doi/10.1021/acs.analchem.2c04554.

Protocol for H&E staining, the parameters for the ATR-FTIR measurement, images of the validation of acini formation, and additional analysis on MCF10A, M2, and M3 acini with FTIR spectroscopic imaging (PDF)

AUTHOR INFORMATION

Corresponding Author

Rohit Bhargava − *Departments of Bioengineering, Electrical and Computer Engineering, Mechanical Science and Engineering, Chemical and Biomolecular Engineering, and Chemistry, Beckman Institute for Advanced Science and Technology, Cancer Center at Illinois, University of Illinois at Urbana-Champaign, Urbana, Illinois 61801, United States;* orcid.org/0000-0001-7360-994X; Email: rxb@illinois.edu

Authors

Pei-Hsuan Hsieh − *Department of Bioengineering and Beckman Institute for Advanced Science and Technology, University of Illinois at Urbana-Champaign, Urbana, Illinois 61801, United States*

Yamuna Phal − *Department of Electrical and Computer Engineering and Beckman Institute for Advanced Science and Technology, University of Illinois at Urbana-Champaign, Urbana, Illinois 61801, United States*

Kannanganattu V. Prasanth − *Department of Cell and Developmental Biology, University of Illinois at Urbana-Champaign, Urbana, Illinois 61801, United States*

Complete contact information is available at: https://pubs.acs.org/10.1021/acs.analchem.2c04554

Notes

The authors declare no competing financial interest.

ACKNOWLEDGMENTS

Research reported in this publication was supported by the National Institute of Biomedical Imaging and Bioengineering of the National Institutes of Health (NIH) under Award Numbers T32EB019944 and R01EB009745 to R.B. K.V.P. laboratory is supported by grants from NIH [AG065748 and GM132458], NSF [EAGER, 1723008], the Cancer Center at Illinois seed grants, and the Prairie Dragon Paddlers. The content is solely the responsibility of the authors and does not necessarily represent the official views of the NIH. Also, P.-H.H. thanks Dr. Mark Gryka for the advice on 3D cell cultures and Dr. Hui Xu, with the Cancer Center at IllinoisTumor Engineering and Phenotyping Shared Resource, on performing DNA extraction.

REFERENCES

(1) Bhargava, R. *Appl. Spectrosc.* **2012**, *66*, 1091−1120.

(2) Diem, M.*Modern Vibrational Spectroscopy and Micro-Spectroscopy: Theory, Instrumentation and Biomedical Applications*; Wiley, 2015; pp 1−443.

(3) Petibois, C.; Déléris, G. *Trends Biotechnol.* **2006**, *24*, 455−462.

(4) Holman, H.-Y. N.; Bechtel, H. A.; Hao, Z.; Martin, M. C. *Anal. Chem.* **2010**, *82*, 8757−8765.

(5) Finlayson, D.; Rinaldi, C.; Baker, M. J. *Anal. Chem.* **2019**, *91*, 12117−12128.

(6) Kumar, S.; Desmedt, C.; Larsimont, D.; Sotiriou, C.; Goormaghtigh, E. *Analyst* **2013**, *138*, 4058−4065.

(7) Doherty, J.; Cinque, G.; Gardner, P. *Appl. Spectrosc. Rev.* **2017**, *52*, 560−587.

(8) Kwak, J. T.; Reddy, R.; Sinha, S.; Bhargava, R. *Anal. Chem.* **2012**, *84*, 1063−1069.
(9) Tiwari, S.; Zong, X.; Holton, S. E.; Prasanth, Kv.; Bhargava, R. *SPIE Proc.* **2015**, *9417*, No. 941720.
(10) Boydston-White, S.; Romeo, M.; Chernenko, T.; Regina, A.; Miljković, M.; Diem, M. *Biochim. Biophys. Acta* **2006**, *1758*, 908−914.
(11) Mohlenhoff, B.; Romeo, M.; Diem, M.; Wood, B. R. *Biophys. J.* **2005**, *88*, 3635−3640.
(12) Romeo, M.; Mohlenhoff, B.; Diem, M. *Vib. Spectrosc.* **2006**, *42*, 9.
(13) Köhler, A.; Sulé-Suso, J.; Sockalingum, G. D.; Tobin, M.; Bahrami, F.; Yang, Y.; Pijanka, J.; Dumas, P.; Cotte, M.; van Pittius, D. G.; Parkes, G.; Martens, H. *Appl. Spectrosc.* **2008**, *62*, 259−266.
(14) Thu, K. L.; Soria-Bretones, I.; Mak, T. W.; Cescon, D. W. *Cell Cycle* **2018**, *17*, 1871−1885.
(15) Underhill, G. H.; Peter, G.; Chen, C. S.; Bhatia, S. N. *Annu. Rev. Cell Dev. Biol.* **2012**, *28*, 385−410.
(16) Katt, M. E.; Placone, A. L.; Wong, A. D.; Xu, Z. S.; Searson, P. C. *Front. Bioeng. Biotechnol.* **2016**, *4*, 12.
(17) Colella, G.; Fazioli, F.; Gallo, M.; De Chiara, A.; Apice, G.; Ruosi, C.; Cimmino, A. *Int. J. Mol. Sci.* **2018**, *19*, 615.
(18) Qu, Y.; Han, B.; Yu, Y.; Yao, W.; Bose, S.; Karlan, B. Y.; Giuliano, A. E.; Cui, X. *PLoS One* **2015**, *10*, No. e0131285.
(19) Debnath, J.; Brugge, J. S. *Nat. Rev. Cancer* **2005**, *5*, 675−688.
(20) Debnath, J.; Muthuswamy, S. K.; Brugge, J. S. *Methods* **2003**, *30*, 256−268.
(21) Eastman, A. E.; Guo, S. *FEBS Lett.* **2020**, *594*, 2084−2098.
(22) Lagies, S.; Schlimpert, M.; Neumann, S.; Wäldin, A.; Kammerer, B.; Borner, C.; Peintner, L. *Commun. Biol.* **2020**, *3*, 246.
(23) Patra, B.; Peng, C. C.; Liao, W. H.; Lee, C. H.; Tung, Y. C. *Sci. Rep.* **2016**, *6*, No. 21061.
(24) Spoerri, L.; Beaumont, K. A.; Anfosso, A.; Haass, N. K. *Methods Mol. Biol.* **2017**, *1612*, 401−416.
(25) Yano, S.; Tazawa, H.; Kagawa, S.; Fujiwara, T.; Hoffman, R. M. *Cancers* **2020**, *12*, 2655.
(26) Blasi, T.; Hennig, H.; Summers, H. D.; Theis, F. J.; Cerveira, J.; Patterson, J. O.; Davies, D.; Filby, A.; Carpenter, A. E.; Rees, P. *Nat. Commun.* **2016**, *7*, No. 10256.
(27) Zucchiatti, P.; Mitri, E.; Kenig, S.; Billè, F.; Kourousias, G.; Bedolla, D. E.; Vaccari, L. *Anal. Chem.* **2016**, *88*, 12090−12098.
(28) Bedolla, D. E.; Kenig, S.; Mitri, E.; Storici, P.; Vaccari, L. *Vib. Spectrosc.* **2014**, *75*, 127−135.
(29) Bedolla, D. E.; Kenig, S.; Mitri, E.; Ferraris, P.; Marcello, A.; Grenci, G.; Vaccari, L. *Analyst* **2013**, *138*, 4015−4021.
(30) Diem, M.; Boydston-White, S.; Chiriboga, L. *Appl. Spectrosc.* **1999**, *53*, 148A−161A.
(31) Boydston-White, S.; Gopen, T.; Houser, S.; Bargonetti, J.; Diem, M. *Biospectroscopy* **1999**, *5*, 219−227.
(32) Boydston-White, S.; Chernenko, T.; Regina, A.; Miljković, M.; Matthäus, C.; Diem, M. *Vib. Spectrosc.* **2005**, *38*, 169−177.
(33) Phal, Y.; Yeh, K.; Bhargava, R. *Anal. Chem.* **2021**, *93*, 1294.
(34) De Meutter, J.; Goormaghtigh, E. *Anal. Chem.* **2021**, *93*, 3733−3741.
(35) Phal, Y.; Yeh, K.; Bhargava, R. *Appl. Spectrosc.* **2021**, *75*, 1067−1092.
(36) Bird, B.; Miljković, M.; Remiszewski, S.; Akalin, A.; Kon, M.; Diem, M. *Lab. Invest.* **2012**, *92*, 1358−1373.
(37) Mittal, S.; Yeh, K.; Leslie, L. S.; Kenkel, S.; Kajdacsy-Balla, A.; Bhargava, R. *Proc. Natl. Acad. Sci. U.S.A.* **2018**, *115*, 5651−5660.
(38) Baker, M. J.; Trevisan, J.; Bassan, P.; Bhargava, R.; Butler, H. J.; Dorling, K. M.; Fielden, P. R.; Fogarty, S. W.; Fullwood, N. J.; Heys, K. A.; Hughes, C.; Lasch, P.; Martin-Hirsch, P. L.; Obinaju, B.; Sockalingum, G. D.; Sulé-Suso, J.; Strong, R. J.; Walsh, M. J.; Wood, B. R.; Gardner, P.; Martin, F. L. *Nat. Protoc.* **2014**, *9*, 1771−1791.
(39) Miller, L. M.; Bourassa, M. W.; Smith, R. J. *Biochim. Biophys. Acta* **2013**, *1828*, 2339−2346.
(40) Morrish, R. B.; Hermes, M.; Metz, J.; Stone, N.; Pagliara, S.; Chahwan, R.; Palombo, F. *Front. Cell Dev. Biol.* **2019**, *7*, 141.
(41) Srisongkram, T.; Weerapreeyakul, N.; Thumanu, K. *Int. J. Mol. Sci.* **2020**, *21*, 4141.
(42) Smolina, M.; Goormaghtigh, E. *Biomed. Spectrosc. Imaging* **2016**, *5*, 155−166.
(43) Smolina, M.; Goormaghtigh, E. *Analyst* **2016**, *141*, 620−629.
(44) Santner, S. J.; Dawson, P. J.; Tait, L.; Soule, H. D.; Eliason, J.; Mohamed, A. N.; Wolman, S. R.; Heppner, G. H.; Miller, F. R. *Breast Cancer Res. Treat.* **2001**, *65*, 101−110.
(45) Schubert, J. M.; Mazur, A. I.; Bird, B.; Miljković, M.; Diem, M. *J. Biophotonics* **2010**, *3*, 588.
(46) Lee, G. Y.; Kenny, P. A.; Lee, E. H.; Bissell, M. J. *Nat. Methods* **2007**, *4*, 359−365.
(47) Schindelin, J.; Arganda-Carreras, I.; Frise, E.; Kaynig, V.; Longair, M.; Pietzsch, T.; Preibisch, S.; Rueden, C.; Saalfeld, S.; Schmid, B.; Tinevez, J. Y.; White, D. J.; Hartenstein, V.; Eliceiri, K.; Tomancak, P.; Cardona, A. Fiji. *Nat. Methods* **2012**, *9*, 676−682.
(48) Reddy, R. K.; Walsh, M. J.; Schulmerich, M.; Carney, P. S.; Bhargava, R. *Appl. Spectrosc.* **2013**, *67*, 93−105.
(49) Nasse, M. J.; Walsh, M. J.; Mattson, E. C.; Reininger, R.; Kajdacsy-Balla, A.; MacIas, V.; Bhargava, R.; Hirschmugl, C. J. *Nat. Methods* **2011**, *8*, 413−416.
(50) Hermes, M.; Morrish, R. B.; Huot, L.; Meng, L.; Junaid, S.; Tomko, J.; Lloyd, G. R.; Masselink, W. T.; Tidemand-Lichtenberg, P.; Pedersen, C.; et al. *J. Opt.* **2018**, *20*, No. 023002.
(51) Brereton, R. G.; Lloyd, G. R. *J. Chemom.* **2014**, *28*, 213−225.
(52) Chen, G.; Deng, X. *Bio-Protocols* **2018**, *8*, 2994.
(53) Mourant, J. R.; Yamada, Y. R.; Carpenter, S.; Dominique, L. R.; Freyer, J. P. *Biophys. J.* **2003**, *85*, 1938−1947.
(54) Lee, J.; Gazi, E.; Dwyer, J.; Brown, M. D.; Clarke, N. W.; Nicholson, J. M.; Gardner, P. *Analyst* **2007**, *132*, 750−755.
(55) Bassan, P.; Byrne, H. J.; Bonnier, F.; Lee, J.; Dumas, P.; Gardner, P. *Analyst* **2009**, *134*, 1586−1593.
(56) Bhargava, R.; Wang, S. Q.; Koenig, J. L. *Appl. Spectrosc.* **1998**, *52*, 323−328.
(57) Wang, Y.; Dai, W.; Liu, Z.; Liu, J.; Cheng, J.; Li, Y.; Li, X.; Hu, J.; Lü, J. *Anal. Chem.* **2021**, *93*, 671−676.
(58) Serec, K.; Šegedin, N.; Krajačić, M.; Babić, S. D. *Appl. Sci.* **2021**, *11*, 2360.
(59) Wood, B. R. *Chem. Soc. Rev.* **2016**, *45*, 1980−1998.
(60) Whelan, D. R.; Bambery, K. R.; Heraud, P.; Tobin, M. J.; Diem, M.; McNaughton, D.; Wood, B. R. *Nucleic Acids Res.* **2011**, *39*, 5439−5448.
(61) Al-Jorani, K.; Rüther, A.; Martin, M.; Haputhanthri, R.; Deacon, G. B.; Li, H. L.; Wood, B. R. *Sensors* **2018**, *18*, 4297.
(62) Traganos, F.; Darzynkiewicz, Z.; Melamed, M. R. *Cytometry* **2005**, *2*, 212−218.
(63) Benedetti, E.; Bramanti, E.; Benedetti, E.; Papineschi, F.; Rossi, I. *Appl. Spectrosc.* **1997**, *51*, 792−797.
(64) Banyay, M.; Sarkar, M.; Gräslund, A. *Biophys. Chem.* **2003**, *104*, 477−488.
(65) Susi, H.; Ard, J. S. *Spectrochim. Acta, Part A* **1971**, *27*, 1549−1562.
(66) Bhargava, R.; Fernandez, D. C.; Hewitt, S. M.; Levin, I. W. *Biochim. Biophys. Acta* **2006**, *1758*, 830−845.
(67) Kong, R.; Reddy, R. K.; Bhargava, R. *Analyst* **2010**, *135*, 1569−1578.
(68) Holton, S. E.; Bergamaschi, A.; Katzenellenbogen, B. S.; Bhargava, R. *PLoS One* **2014**, *9*, No. e96878.
(69) Ukkonen, H.; Kumar, S.; Mikkonen, J.; Salo, T.; Singh, S. P.; Koistinen, A. P.; Goormaghtigh, E.; Kullaa, A. M. *Vib. Spectrosc.* **2015**, *79*, 24−30.
(70) Smolina, M.; Goormaghtigh, E. *Analyst* **2018**, *143*, 2520−2530.
(71) Smolina, M.; Goormaghtigh, E. *Analyst* **2015**, *140*, 2336−2343.
(72) Menon, S. S.; Guruvayoorappan, C.; Sakthivel, K. M.; Rasmi, R. R. *Clin. Chim. Acta* **2019**, *491*, 39−45.
(73) Vaapil, M.; Helczynska, K.; Villadsen, R.; Petersen, O. W.; Johansson, E.; Beckman, S.; Larsson, C.; Påhlman, S.; Jögi, A. *PLoS One* **2012**, *7*, No. e46543.

https://doi.org/10.1021/acs.analchem.2c04554
Anal. Chem. XXXX, XXX, XXX−XXX

(74) Debnath, J.; Mills, K. R.; Collins, N. L.; Reginato, M. J.; Muthuswamy, S. K.; Brugge, J. S. *Cell* **2002**, *111*, 29−40.
(75) Gaiko-Shcherbak, A.; Fabris, G.; Dreissen, G.; Merkel, R.; Hoffmann, B.; Noetzel, E. *PLoS One* **2015**, *10*, No. e145174.
(76) Petibois, C.; Desbat, B. *Trends Biotechnol.* **2010**, *28*, 495−500.
(77) Whelan, D. R.; Bambery, K. R.; Puskar, L.; McNaughton, D.; Wood, B. R. *Analyst* **2013**, *138*, 3891−3899.
(78) Wang, Y.; Dai, W.; Liu, Z.; Liu, J.; Cheng, J.; Li, Y.; Li, X.; Hu, J.; Lü, J. *Anal. Chem.* **2021**, *93*, 671−676.

https://doi.org/10.1021/acs.analchem.2c04554
Anal. Chem. XXXX, XXX, XXX−XXX